nature electronics

Article

https://doi.org/10.1038/s41928-022-00843-6

A stretchable epidermal sweat sensing platform with an integrated printed battery and electrochromic display

Received: 15 December 2021

Accepted: 30 August 2022

Published online: 6 October 2022

Check for updates

Lu Yin[1,3], Mengzhu Cao[1,3], Kyeong Nam Kim[1,3], Muyang Lin[1], Jong-Min Moon[1], Juliane R. Sempionatto[1], Jialu Yu[1], Ruixiao Liu[1], Connor Wicker[1], Alexander Trifonov[1], Fangyu Zhang[1], Hongjie Hu[1], Jose R. Moreto[1], Jaekyung Go[2], Sheng Xu[1] and Joseph Wang[1]

Wearable electronic devices are of potential use in various health monitoring applications including non-invasive chemical sensing. However, such platforms are typically limited by the need to connect to external devices for power and data visualization. Here we report a stretchable epidermal sweat sensing platform that integrates a stretchable battery and a low-power digital electrochromic display. The patch can operate as a standalone device to directly display the concentration of various electrolytes or metabolites in sweat, such as glucose and lactate, without any wired or wireless connection to external devices. It consists of electrochemical sensors, a stretchable Ag_2O–Zn battery, ten individually addressable electrochromic pixels and a small microcontroller unit. All the components and interconnections, except the microcontroller, are fabricated via the high-throughput screen printing of customized elastomeric or silver inks. The integrated system is robust to mechanical deformation and is unaffected by 1,500 stretching cycles at 20% strain. The electrochromic display exhibits stability for 10,000 on/off cycles, and the battery can power 14,000 sensing sessions over a week-long use.

Soft electronics are of use in on-body sensing and human–machine interfacing[1–4]. Integrated epidermal sensing systems have, for instance, been developed as 'labs on the skin' for recording various mechanical, electrical, physiological and electrochemical signals[5–8]. In particular, epidermal sweat sensing with electrochemical sensors can be used to detect electrolytes, metabolites, nutrients and drugs, providing non-invasive health monitoring for precision medicine, personalized nutrition and sports performance[6–9]. The development of wearable sensors for such applications is increasingly moving away from separate physical and chemical sensors, and towards the integration of sensors with electronics for energy management, signal acquisition and data interfacing[9–14]. However, most wearable electronics currently operate with commercial lithium polymer pouches or coin cells, which are rigid, unsafe and add bottlenecks to the product design. Conformal epidermal sensors with wired connections or short-range wireless power delivery have been designed to avoid battery-related limitations, but these can compromise the autonomy of the system and limit user mobility[9,11,15–18].

Integrated sensors also typically rely on wireless data transmissions, which require external devices (such as computers, smartphones and receivers) for users to obtain the sensing results[9,11,19–21]. A lack of direct access to sensing results means that many existing wearable sensors can be inconvenient in practical applications. Skin-conformal flexible electronic systems that include visual data presentation could

[1]Department of Nanoengineering, University of California San Diego, La Jolla, CA, USA. [2]Samsung Display, Yongin-si, South Korea. [3]These authors contributed equally: Lu Yin, Mengzhu Cao, Kyeong Nam Kim. e-mail: josephwang@ucsd.edu

address these limitations, simplify designs and improve user experience. There are, however, major barriers to integrate accurate on-body sensing and real-time display capabilities within a compact, flexible and wearable monitoring platform[22].

Conventional display technologies can be modified to have flexible form factors for wearable electronics, but their high power consumption limits application in compact low-energy electronic systems[35–37]. Alternatively, non-emissive displays, such as liquid crystal and electronic ink displays controlled by a microcontroller, consume low power and can effectively present data. However, their lack of flexibility and stretchability limits integration with wearable devices[23,38]. Nevertheless, integrated sensing systems with miniaturized display elements have been developed for visualizing data in real time for direct readout[13,14,23–26]. These include colorimetric assays that directly react with the target analytes (such as glucose or chloride ions) and qualitatively report the results via the naked eye[27]. Electrochromic materials that change their colour or opacity by applying an electrical potential have also been integrated with sensing systems for data visualization[28–31]. However, colorimetric display technologies have long reaction times, and naked-eye readout lacks spatial and colorimetric resolution, resulting in inaccurate and unclear data presentation. Further analysis is usually required to convert qualitative colorimetric information into numerical data using smartphones, spectral analysers or cameras[24,26,32–34].

In this Article, we report an epidermal sensing platform with an integrated electrochromic display (ECD) for the real-time visualization of analytical data and a high-performance stretchable battery for power supply. The epidermal patch consists of stretchable enzymatic and potentiometric electrochemical sensors for sensing various metabolites and electrolytes in sweat, a stretchable Ag_2O–Zn battery, ten fast responding and reversible poly(3,4-ethylene dioxythiophene) polystyrene sulfonate (PEDOT:PSS)-based electrochromic pixels and a low-power microcontroller unit (MCU) chip (Supplementary Video 1). All the sensors, batteries and ECDs are fabricated via the high-throughput screen printing of customized stretchable composite inks on a heat-sealable thermoelastic styrene–ethylene–butylene–styrene (SEBS) block co-polymer substrate (Fig. 1a and Supplementary Fig. 1). Electrical connections between the components of the system and with the MCU are printed using stretchable silver ink layers treated with a chloride/lactate acid treatment[39], which exhibit stable electrical connections under repeated stretching (Supplementary Fig. 2).

The system is solely powered by the integrated battery, which is activated by a switch that connects the batteries to the MCU. The signal input from the electrochemical sensor is then sampled by the MCU via an analogue-to-digital converter (ADC), which converts the analytical data into digital outputs that control the on and off states of the ten ECD pixels (Fig. 1b). As the sensor relies on potentiometric reading when in contact with the analyte and independently operates from the MCU, the sensing and data visualization occur in under one second once the switch is pressed. We illustrate the capabilities of the integrated system using two potentiometric sweat sensors for monitoring sodium ions and pH, and two enzymatic amperometric sweat sensors for monitoring glucose and lactate, with the analyte concentrations displayed on the ECD (Fig. 1c). The epidermal patch exhibits excellent durability and mechanical robustness (Fig. 1d(i),(ii)), demonstrating 10,000 sensing sessions over five days and 1,500 stretching cycles at 20% strain without affecting its sensing or display capability. A rapid room-temperature 'solvent-welding' process was developed to bond the rigid chip and soft printed circuit, which have very different elastic moduli; consequently, the MCU can be securely connected without using conductive adhesives (Fig. 1d(iii) and Supplementary Fig. 3). The use of maleic-anhydrite-grafted SEBS (SEBS-MA) further strengthens the bonding of the MCU metal contact pads to the substrate, allowing up to 300% strain without detachment (Supplementary Fig. 4).

Stretchable PEDOT:PSS ECDs

Integrating ECDs into skin-interfaced electronic systems provides timely data visualization, such as the level of a target biomarker in the case of on-body sensing platforms. Our skin-interfaced integrated sensing platform features a dedicated and highly responsive low-power ECD for the direct visualization of analytical data. The ECD was chosen for its low power consumption compared with light-emitting display technologies, as it features low self-discharge and only requires energy as the displaying content is refreshed. The electrochromic PEDOT:PSS electrode material was selected for its stretchability and compatibility with screen-printing processes. Fabricated via layer-by-layer screen printing, the ECD was composed of a top PEDOT:PSS panel and ten separately addressable pixels on the bottom panel, with a highly viscous polystyrene sulfonate (PSS)-based electrolyte used to create ionic pathways between the two panels as the opposing electrodes are physically separated; stretchable and printed silver traces were used to connect the ECD to the MCU and were covered with an insulating elastomer layer to avoid short-circuiting and corrosion (Fig. 2a and Supplementary Fig. 1). The colour of the PEDOT:PSS conducting polymer is dependent on its redox state, as described in the half-reaction below.

$$(\mathrm{PEDOT})^{+}\,(\mathrm{PSS})^{-}\,(\text{light blue}) + \mathrm{e}^{-} \leftrightarrow \mathrm{PEDOT}\,(\text{dark blue}) + \mathrm{PSS}^{-} \quad (1)$$

The colour change, thus, occurs on the front panel during the reductive PSS-undoping process on applying a potential above 1 V between the two electrodes, during which the reverse oxidative doping process takes place on the back-panel PEDOT:PSS electrodes. Thus, to induce a colour change, a positive potential can be applied to the bottom pixels, which results in the colour-changing reduction of PEDOT:PSS within the corresponding region on the front panel covered by the block of PSS electrolyte (Fig. 2b and Supplementary Fig. 5). The printable PEDOT:PSS ink was optimized for stretchability and compatibility with the elastic SEBS substrate and shows excellent mechanical behaviour and electrochemical stability on repeated 20% stretching deformation (Fig. 2c and Supplementary Fig. 6). Cyclic voltammetry of the electrochromic pixel was carried out with scan rates of 0.1, 0.5 and 1.0 V s^{-1} over the 0–1.5 V range (Fig. 2d). The on/off switching of the ECD was characterized using potential stepping between 0 V and a set switching voltage as the current was monitored. As shown in Fig. 2e, Supplementary Figs. 6 and 7 and Supplementary Video 3, a switching voltage of 1.5 V was determined to be optimal as it results in the fastest turn-on response with a turn-off response below 500 ms. In comparison, the 1 V switching voltage resulted in a slower turn-on and turn-off speed, whereas switching voltages of 2 and 3 V, as a fast turn-on rate is given, led to a slower turn-off speed due to excessive charge accumulation on the electrodes. Such a high voltage can also lead to electrolyte breakdown as well as irreversible electrode overoxidation that limits the cycle life of the electrochromic cells and should be avoided. The average power consumption of turning on each pixel, on applying the optimal 1.5 V for 1 s, was determined to be 0.08 mW (Supplementary Fig. 8). This behaviour was examined again after 1,500 cycles of repeated 20% uniaxial stretching along two orthogonal directions. The results (Fig. 2f, Supplementary Fig. 9 and Supplementary Video 2) demonstrate a slightly reduced turn-on and turn-off current but a negligible change in switching speed, indicating the excellent stretchability of the PEDOT:PSS electrodes. As characterized via electrochemical impedance spectroscopy (Fig. 2g), the reduction in switching current can be attributed to a slight increase (<200 Ω) in the electrode serial resistance, whereas the charge transfer and diffusion impedance remained mostly constant. The electrochemical stability of the ECD was tested via repeated cycling of the PEDOT:PSS electrodes between on and off (Fig. 2h(i)) over 10,000 cycles (Fig. 2h(ii)) via potential steps between 0 and 1.5 V. The electrical current response of the pixel shows high reproducibility with only 17% decrease in the peak current after

https://doi.org/10.1038/s41928-022-00843-6

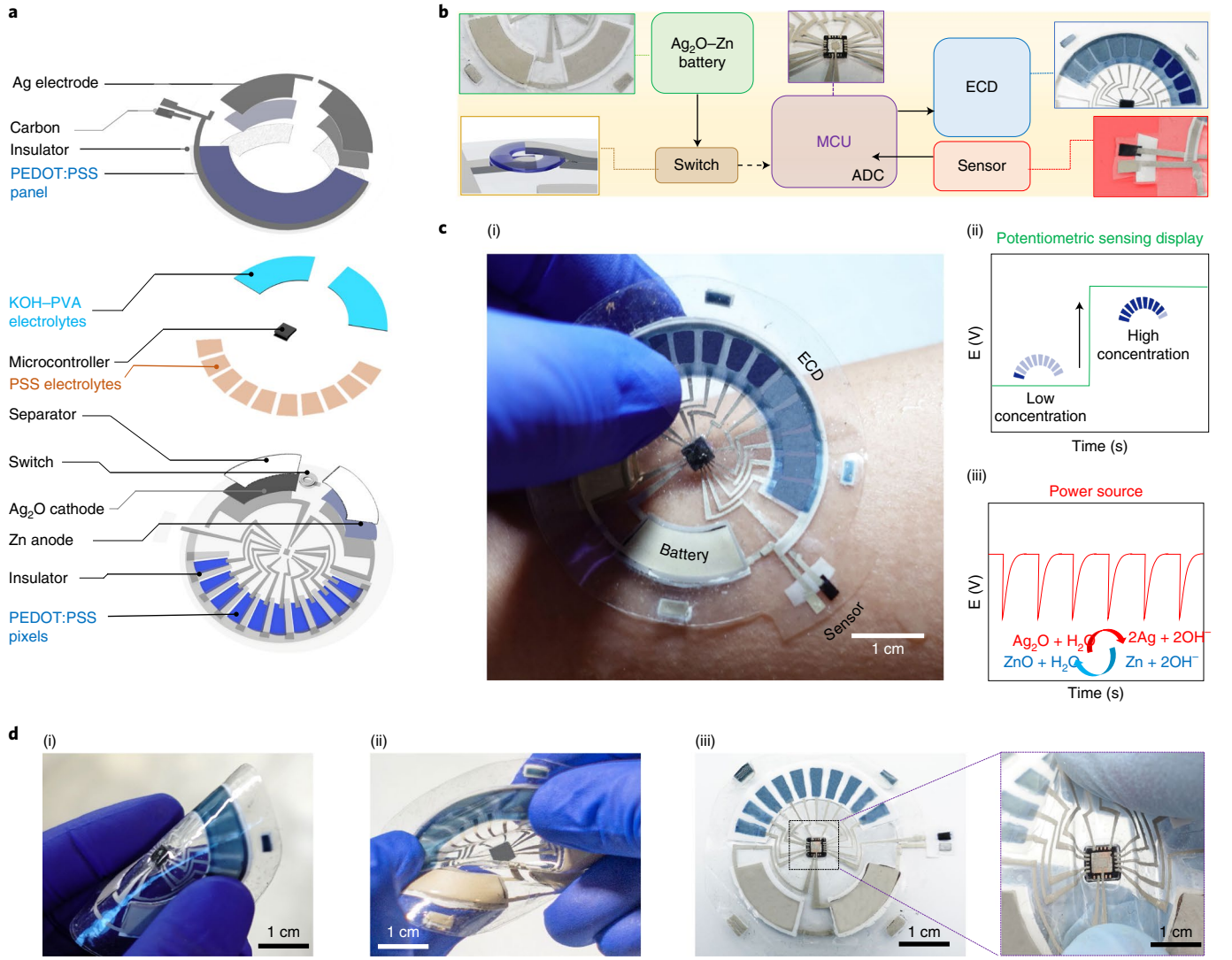

Fig. 1 | System overview of the all-printed skin-interfaced ECD sensing patch. **a**, Exploded view detailing the individual layers of the epidermal patch. The detailed fabrication procedures are provided in the Supplementary Information. **b**, System flow chart of the system and the zoomed-in view of the individual modules. **c**, Operation of the patch. Photographic image demonstrates the patch used for epidermal sweat sensing by instantaneously revealing the target concentration (i). Illustration of the change in display that changes with the electrolyte concentration and readout of the potentiometric sensor (ii) and the intermittent discharge mode of the Ag_2O–Zn battery that supplies power to the system (iii). **d**, Photographic images demonstrating the mechanical performance and durability of the patch, including its bending (i) or stretching (ii) and stretching of the connection between the interconnect and MCU (iii).

about 10,000 on/off cycles (Fig. 2h(iii),(iv) and Supplementary Fig. 10), which can be caused by the increased cell impedance due to electrode overoxidation from repeated cycling (Supplementary Fig. 11). Such high mechanical and electrochemical stabilities ensure the continued and reliable operation of the ECD within the designed lifetime of the system.

Battery performance

The all-printed fabrication of the flexible Ag_2O–Zn battery was designed based on the selection of substrate and ink formulation that ensures mechanical stretchability, electrochemical stability, chemical resiliency, operational safety, light weight and comfort. SEBS was selected as the binder for electrodes, separator and substrate due to its chemical stability in the alkaline electrolyte used in the Ag_2O–Zn battery. Furthermore, thermoelastomeric SEBS is compatible with both heat and vacuum sealing, which grants reliable packaging to protect and contain the electrolyte. Polyvinyl alcohol (PVA) hydrogel electrolyte infused with 9 M potassium hydroxide was also formulated to physically contain the electrolyte and avoid leakage. A stacking configuration was designed to minimize the device footprint as the ion diffusion distance between the battery electrodes is reduced for minimizing the internal resistance. The batteries, with the customized silver current collector, zinc anode, Ag_2O cathode and titanium dioxide (TiO_2) separator inks, were printed in a layer-by-layer manner on the top and bottom panels and assembled via heat and vacuum sealing on placing the electrolyte hydrogel (Fig. 3a). The redox reaction of the resulting Ag_2O–Zn battery relies on the dissolution of zinc ions (Zn^{2+}) and silver ions (Ag^{+}) in the alkaline electrolyte and their supersaturation-induced precipitation, which takes place rapidly as a stable voltage is maintained at 1.56 V (Fig. 3b). The reactions are described below (E, electrode potential; SHE, standard hydrogen electrode).

$$\text{Anode}: Zn + 2OH^- \leftrightarrow ZnO + H_2O + 2e^- \quad E = -1.22\ \text{V versus SHE} \tag{2}$$

$$\text{Cathode}: Ag_2O + H_2O + 2e^- = 2Ag + 2OH^- \quad E = +0.34\ \text{V versus SHE} \tag{3}$$

https://doi.org/10.1038/s41928-022-00843-6

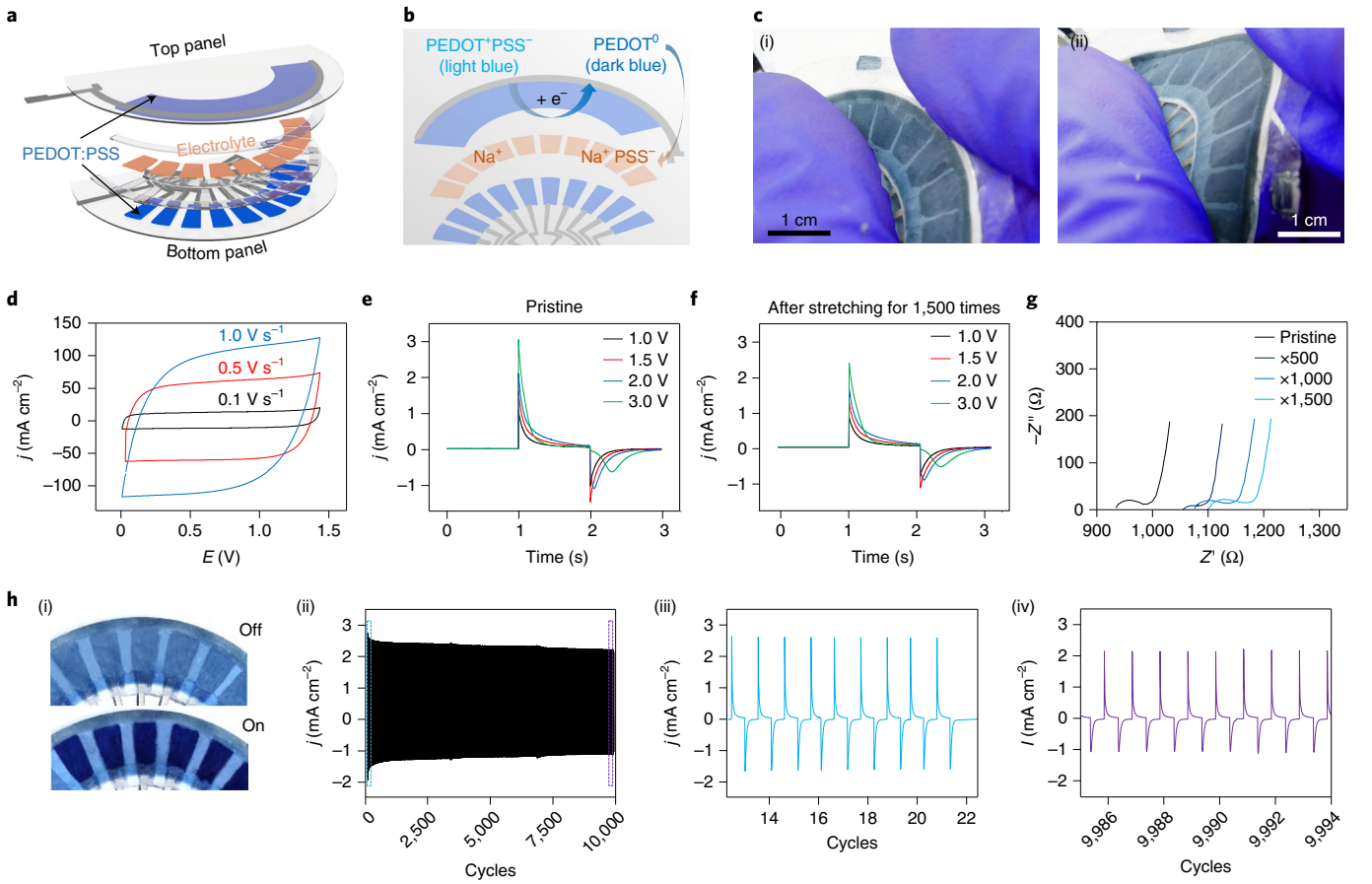

Fig. 2 | Characterization of ECD. a, Exploded view of the individual layers of the ECD display. **b**, Reaction mechanism of the ECD display. **c**, Photographic images of the ECD display before (i) and during (ii) stretching. **d**, Cyclic voltammetry of an ECD pixel at increasing scan rates of 0.1–1.0 V s^{-1}. **e**, Turn-on and turn-off currents for pristine ECD pixels at different voltages. **f**, Turn-on and turn-off currents for ECD pixels at different voltages after stretching 1,500 times. **g**, Electrochemical impedance spectroscopy profile of a pixel before and after stretching 500, 1,000 and 1,500 times. **h**, Photographic images of the ECD pixels in the 'off' and 'on' states (i). Stability of the current profile of the ECD pixel with turn on and turn off for 10,000 cycles (ii) and the zoomed-in views of the current fluctuations for the 14–22 cycles (iii) and 9,986–9,994 cycles (iv).

The capacity of the printed stretchable battery can be adjusted by the loading of cathode material, as controlled by the number of layers of printing. As shown in Fig. 3c, batteries with different (1–4) layers of printed cathode were prepared and tested at the discharge rate of 1 mA cm^{-2}. Such a thickness change results in a proportional increase in capacity with the number of layers, reaching as high as 11.5 mAh cm^{-2} with four layers of cathode loading. The power consumption of the MCU was separately characterized at various operation potentials, and the current draw at the voltage of 1.5 V was determined to be at roughly 1 mA (Supplementary Fig. 13). The operation of the system was tested with 1 s of discharge at 1 mA discharge every 30 s, which simulates the repeated sensing and display sessions on pressing the switch mechanism. As shown in Fig. 3d, the battery (with two layers of cathode) is able to deliver a stable voltage with a constant small ohmic drop throughout the continued usage of the device, indicating a constant cell impedance over its entire range of state of charge. Using this simulated discharge profile—where the sensor is used twice every minute—the system can provide energy for over 14,000 sensing sessions, corresponding to a service time of over 120 hours. The mechanical stability of the battery under repeated uniaxial stretching was evaluated at 1 mA discharge for 1,500 cycles of 20% uniaxial stretching (Fig. 3e, Supplementary Fig. 14 and and Supplementary Video 1). As shown in Fig. 3f, the increase in ohmic drop due to battery stretching was negligible to the voltage delivered during the continuous 1 mA discharge, thus confirming its mechanical robustness as a reliable power source for the stretchable epidermal sensing platform. Moreover, the shelf life of the battery was tested over 1,000 h, displaying a negligible change in voltage and internal resistance of <40 Ω (Supplementary Fig. 15), reflecting the high chemical stability of the electrodes, electrolyte and packaging materials.

Stretchable display system with potentiometric sensors

Two types of potentiometric sensor, namely, for monitoring pH and sodium, were employed for demonstrating the applicability of the all-in-one sensing device. Both sensors rely on measuring the potential difference between the modified working electrode and silver/silver chloride (Ag/AgCl) reference electrode when in contact with the sample solution (Fig. 4a). Such potentiometric sensing applies to a wide range of clinically or environmentally important electrolytes. By printing the stretchable silver ink and carbon ink on the SEBS substrate, the two-electrode sensor shows satisfactory resiliency to 20% stretching (Fig. 4b(i)(ii)). The electrode–electrolyte interface of the sodium-ion-selective-membrane-modified sodium sensor results in a sodium concentration gradient (between the membrane and solution), leading to a potential signal that logarithmically depends on the sodium concentration (Fig. 4c(i)). Figure 4c(ii) depicts the calibration of the fabricated sodium sensor, demonstrating a slope of 62.4 mV per decade of sodium concentration, with a high correlation coefficient (R^2 = 0.9996), over the 0.1–100.0 mM range. The high selectivity of the sodium sensor is demonstrated by the negligible change in sensor potential response

https://doi.org/10.1038/s41928-022-00843-6

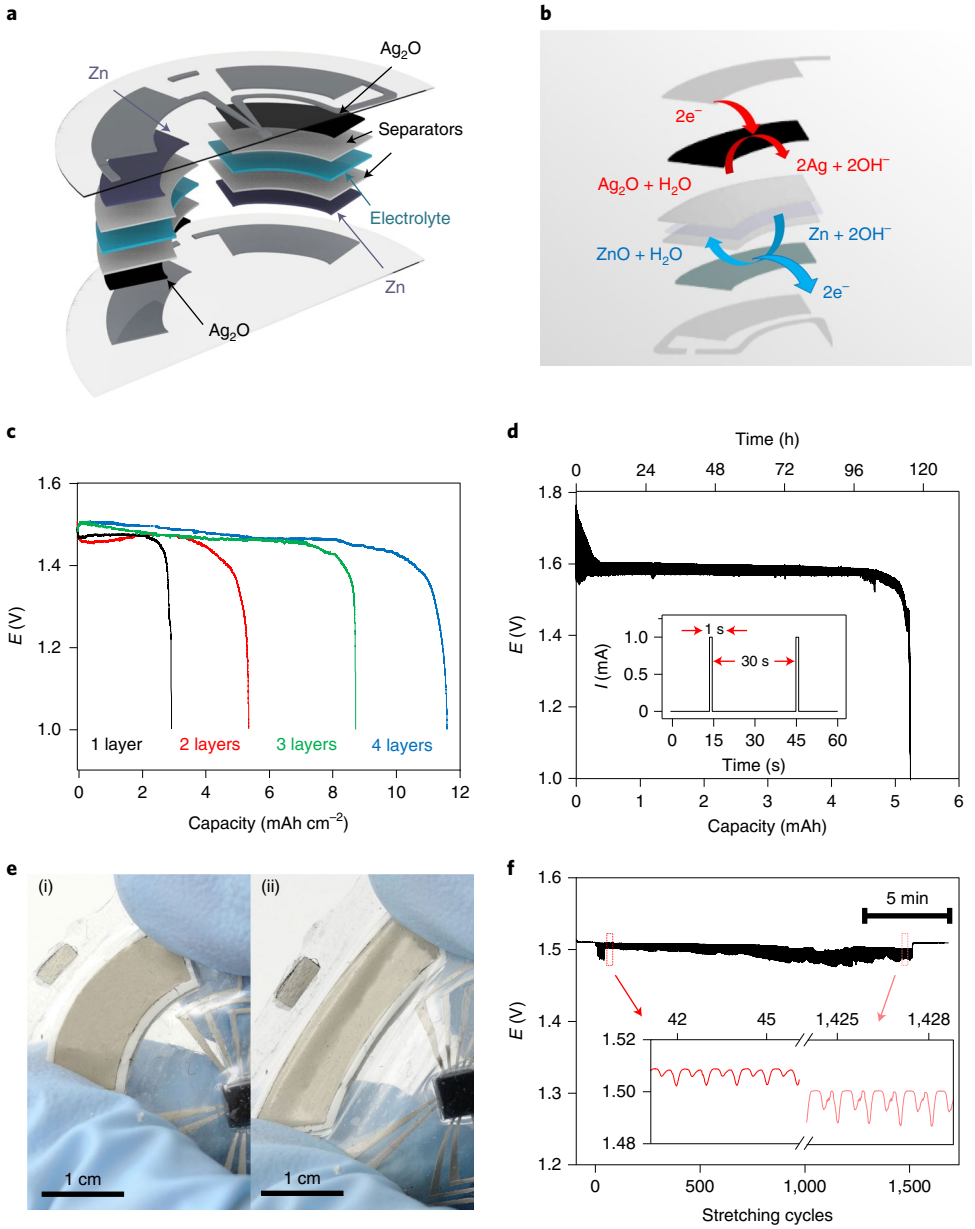

Fig. 3 | Characterization of stretchable battery. a, Exploded view of the individual layers of Ag_2O–Zn battery. The detailed fabrication procedures are provided in the Methods section. **b**, Anode and cathode reaction mechanisms of Ag_2O–Zn battery. **c**, Constant 1 mA discharge of the printed battery with different cathode thicknesses. **d**, Stability of the potential profile of battery discharge at 1 mA cm^{-2} during 108 h with a 30 s resting time. **e**, Photographic images of the battery before (i) and during (ii) stretching. **f**, Stability of the potential profile of battery discharge at 1 mA cm^{-2} for 1,500 stretching cycles and the inset shows the discharge–self-charging curves.

in the presence of potassium and different pH values (Supplementary Fig. 16). As shown in Fig. 4c(iii), the potential response of the sensor in alternating 0.1 and 10.0 mM sodium solutions is highly reversible and exhibits minimal changes after 500, 1,000 and 1,500 stretching cycles, reflecting the excellent stretchability of the sodium sensor.

The pH sensor is fabricated by the electropolymerization of polyaniline onto the working carbon electrode. The operation of the resulting pH sensor is based on the protonation and de-protonation of nitrogen atoms in the polymer chains of polyaniline (Fig. 4d(i)). The sensitivity of the fabricated pH sensor is evaluated by measuring the potential response at pH values in the range of 3–8 (Fig. 4d(i)). The sensors display a linear response of 62.62 mV pH^{-1} with a high correlation coefficient (R^2 = 0.9995) across the entire pH range (Fig. 4d(ii)). As illustrated in Fig. 4d(iii), the modified pH sensor displays excellent stretchability, as evidenced by the highly stable potential signals measured at pH 4 and pH 7, with negligible changes after 500, 1,000 and 1,500 stretching cycles. In addition, the pH sensor demonstrates good selectivity in the presence of Na^+ and K^+ (Supplementary Fig. 16). The operating voltage obtained from sodium and pH sensors is converted into logic outputs, programming the MCU and correlating the obtained voltage values to the display content (Fig. 4e and Supplementary Tables 1 and 2). By integrating the pH sensor with the ECD, we, thus, fabricated an all-in-one epidermal patch for rapid pH sensing and display (Fig. 4f(i)(ii)).

Stretchable display system with enzymatic sensors

Two enzymatic sensors for glucose and lactate were selected to demonstrate the applicability of the integrated ECD patch in a real-life scenario

https://doi.org/10.1038/s41928-022-00843-6

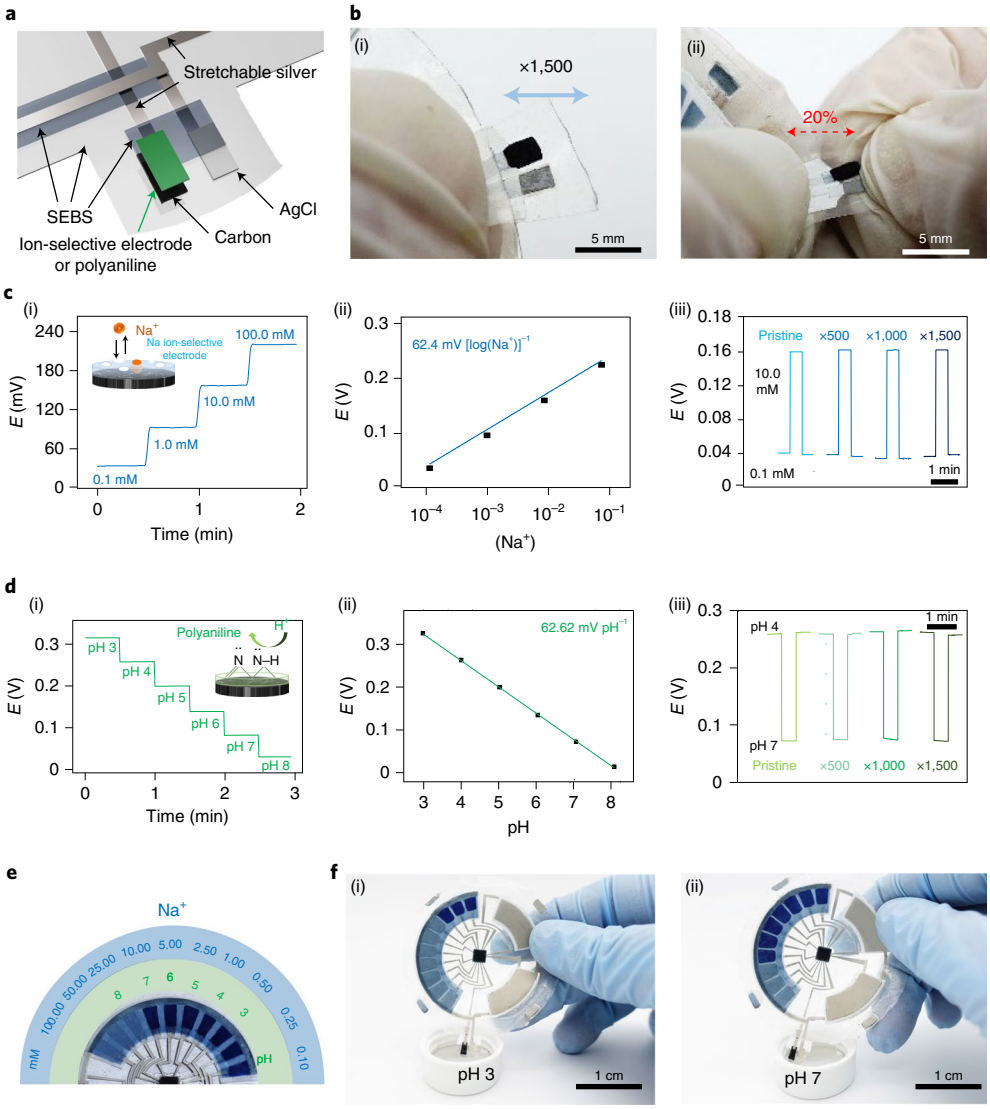

Fig. 4 | Device operation for potentiometric pH and sodium sensing. **a**, Exploded view of the individual layers of potentiometric sensors. **b**, Photographic images of the pH sensor before (i) and during (ii) 20% stretching. **c**, Potentiometric signal obtained in 0.1 M PBS (pH 7.4) on changing the sodium concentration and schematic of the sodium sensor (i). Corresponding calibration plot of the sodium sensor (ii). Open-circuit potential response of the sodium sensor in 0.1 and 100.0 mM NaCl solutions after every 500 times of 20% stretching (iii). **d**, Potentiometric signal obtained in 0.1 M PBS and schematic of the pH sensor (i). Corresponding calibration plot of the pH sensor (ii). Open-circuit potential response of the pH sensor in solutions of pH 4 and pH 7 after every 500 times of 20% stretching (iii). **e**, Illustration of the number of pixels for the ECD patch related to the signals of the pH (green) and sodium (blue) sensors. **f**, Photographic images of the ECD patch reading pH 3 (i) and pH 7 (ii) in 0.5 M PBS.

for epidermal sweat sensing of both metabolites. Both enzymatic sensors commonly rely on amperometric measurements, where the electrical current at a set potential can be correlated to the metabolite concentration using a sigmoidal fitting:

$$E = E_0 - \frac{E_0 - a}{1 - \left(\frac{\text{Conc.}}{b}\right)^c}, \quad (4)$$

where E is the sensor voltage, E_0 is the open-circuit potential of the sensor without load, Conc. is the analyte concentration and a, b and c are constants[40]. To enable rapid and low-power-consumption sensing as the need for potentiostats and amplifiers is obviated and removing them from the circuits, a self-powered sensing mechanism that converts the amperometric signal to a voltage signal was implemented under an optimized load. The sensor electrodes are composed of a printed carbon working electrode along with Ag_2O counter electrode, where the carbon electrodes were thereafter functionalized with the corresponding enzymes for their target analytes (Fig. 5a). Figure 5b displays the lengthwise stretching of the enzymatic sensor fabricated using the customized stretchable inks. As shown in Fig. 5c, the epidermal patch perfectly matches the skin curvature of the subject's forearm. After sweat is induced from the loaded exercise, the subject can mount the integrated system on the forearm for demonstrating its application in real conditions. On pressing the switch for 1 s, the sensor was, thus, able to display the lactate concentration on the wearer's skin without needing any external devices, allowing the user to directly obtain the sensing results without the need of any stabilization time or delay.

The lactate sensor operates based on the selective 1,4-naphthoquinone (NQ)-mediated oxidation of lactate on the working electrode by the lactate oxidase (LOx) enzyme, immobilized on carbon nanotubes. The working electrode is coupled with the Ag_2O

counter electrode that undergoes a high reaction-rate reduction of Ag_2O to Ag, independent of the analyte concentration. On applying a load, a continuous current flows between the enzyme electrode and Ag_2O electrode, which is dominated by the concentration-limited electrocatalytic reaction on the LOx electrode (Fig. 5d(i)). The optimization of the load ensures a maximized signal resolution over the desired concentration region. To this end, linear sweep voltammetry (LSV) was performed at typical sweat lactate concentrations[41–43], namely, 0 and 25 mM, and the potential was plotted against the load (Fig. 5d(ii)). As shown, a load of 75 kΩ was selected, where the potential difference between 0 and 25 mM lactate in artificial sweat (AS) was at the maximum. Subsequently, the in vitro voltage response of the lactate sensor at different concentrations was measured under the 75 kΩ load and fitted with a sigmoidal model (Fig. 5d(iii) and Supplementary Fig. 18d)[40]. To further illustrate the importance of optimizing the load to the range and resolution of the lactate sensor, the sensor was also tested under different loads of 10 and 500 kΩ (Supplementary Fig. 17). This test showed a minimal potential change above the lactate concentration of 10 mM under the 500 kΩ load, and poor voltage resolution across 0–30 mM lactate concentrations under the 10 kΩ load. Figure 5c(iv) examines the stretchability of the lactate sensor, demonstrating highly stable and reversible voltage signal after 1,500 cycles of lengthwise uniaxial 20% stretching. Additional characterization shows that the lactate sensor exhibits effective discrimination against common sweat constituents, including urea, ascorbate, acetaminophen and glucose, as well as high electrochemical stability, operating continuously over 9 hours (Supplementary Fig. 18b). Considering the potentially changing pH of human sweat, the fabricated lactate sensor was tested in different AS scenarios with variable pH values of 5.5, 6.5 and 7.4 (Supplementary Fig. 19). No noticable differences in potentiometric response were observed among the tested samples, demonstrating the reliability and practicality of the sensor. Based on the results obtained from the lactate sensors, the MCU can be programmed to convert the voltage response of the sensors to the 10 pixel digital display within the desired range (Fig. 5e(i) and Supplementary Tables 3 and 4). The on-body application of the epidermal device was demonstrated by integrating the all-in-one lactate sensor system. A sweat-compatible adhesive layer with a simple fluidic design was attached to the back panel of the patch for directing the sweat flow through the sensor and to establish temporal resolution (Supplementary Figs. 23 and 24). The experimental sweat flow data is supported by the theoretical simulation (Supplementary Fig. 24c). Validated using commercial lactate meters, the sensor, thus, shows the ability to track the temporal profile of lactate level in sweat over a given period of time. The observed lactate level changed from the initial 6 mM at the beginning of perspiration to 9 mM after 5 min, reflecting changes in the metabolic activity of the sweat gland (Fig. 5e(ii)(iii)).

Using a similar two-electrode construction, the NQ-mediated glucose oxidase was used to obtain a highly selective glucose-sensing working electrode in connection to the Ag_2O counter electrode (Fig. 5f(i)). The load was similarly optimized via LSV at 75 kΩ and using 0 and 20 mM glucose solutions (Fig. 5f(ii)). The well-defined potential response of the resulting glucose sensor over the 0–10 mM range is presented in Fig. 5f(iii), and its high selectivity against common sweat constituents, including uric acid, ascorbic acid, acetaminophen and lactate, is displayed in Supplementary Fig. 20. The stretchability of the sensor was assessed by stretching the electrode as its potential response to 2.5 and 10.0 mM glucose solutions is recorded. As illustrated in Fig. 5f(iv), the glucose response remained highly stable after 1,500 cycles of lengthwise uniaxial 20% stretching. Similar to the lactate sensor, the glucose sensor was tested in AS under variable pH values, demonstrating a stable voltage signal regardless of the environment, and confirming its practicality under real-life operating conditions (Supplementary Fig. 21). It is worth noting that such current-to-voltage signal conversion can be tailored for accommodating the lower glucose concentration in human sweat. This is accomplished by adjusting the load to a higher value, which enhances the signal resolution in lower concentrations in exchange for a wider range. To this end, an optimized load at 250 kΩ was applied to enhance the voltage difference for glucose concentrations over the 0–5 mM range (Fig. 5f(v)(vi)). Similarly, the load was optimized to 10 MΩ to enhance the difference below 1 mM glucose towards the monitoring of sweat glucose, which is typically below 0.5 mM (Fig. 5f(vii)(viii))[44]. Similarly, the patch with a glucose sensor can be placed on the body to trace the glucose changes over a period of time. Based on the results obtained from the glucose sensors in the 0–0.5 mM range, the MCU was programmed to convert the voltage response of the sensors to the 10 pixel digital display (Fig. 5g(i) and Supplementary Table 6). The glucose level increased after the intake of sugary drinks during exercise, with the trend agreeing with the changes in blood glucose level (Fig. 5g(ii)(iii)).

Conclusions

We have reported an all-printed epidermal monitoring system with a compact, flexible and stretchable form factor for non-invasive sweat monitoring. The integrated system combines sensors, ECDs and batteries and allows users to obtain accurate electrochemical sensing data and directly and rapidly display it during normal activities, without needing to connect to external devices. Stable and robust elastomers were used as the substrate and binder, which allows the components to be fabricated via the low-cost, high-throughput layer-by-layer stencil printing. The ECDs exhibit colour reversibility for over 10,000 on/off sensing cycles and 1,500 stretching cycles at 20% strain, and the battery could power 14,000 discrete sensing sessions. To illustrate the range of sensing options, potentiometric pH and sodium electrolyte sensors as well as enzymatic glucose and lactate metabolic biosensors were shown to be compatible with the integrated sensing platform. The fully autonomous multifunctional self-sustainable wearable sweat sensing platform could be of use in a diverse range of practical applications in personal wellness management, healthcare monitoring and professional sports. Further development of skin-worn monitoring-display platforms and power sources, such as via flexible microgrids[13,45], could offer full autonomy and improved user experience for next-generation wearable monitoring platforms.

Fig. 5 | Device operation for glucose and lactate sensors. a, Exploded view of the individual layers of enzymatic sensors. **b**, Photograph of the lactate sensor before (i) and during (ii) 20% stretching. **c**, Photograph of on-body sensing by placing the ECD patch on the forearm during stationary cycling. **d**, Schematic of the lactate sensing mechanism (i). LSV curves (1 mV s^{-1}) for 0 and 25 mM lactate (1 mV s^{-1}) (ii). Potentiometric signal obtained in 0.1 M AS at pH 7.4, on increasing the lactate concentration from 5 to 30 mM under 75 kΩ load (iii). Potential response in 2.5 and 15.0 mM lactate after every 500 times of 20% stretching (iv). **e**, Number of pixels corresponding to different lactate concentrations (i). Sweat lactate sensing measured using a commercial meter and patch (ii). The patch displays in the range of 0–15 mM. On-body lactate sensing on the subject's forearm and displaying 4.5 and 7.5 mM results by constant-load exercising (iii). **f**, Schematic of the glucose-sensing mechanism (i). LSV curves (1 mV s^{-1}) for 0 and 20 mM glucose (ii). Potentiometric signal obtained in AS at pH 7.4 with 2.5 to 10.0 mM glucose under 75 kΩ load (iii). Sensor response in 2.5 and 10.0 mM glucose solutions after every 500 times of 20% stretching (iv). LSV curves (1 mV s^{-1}) for 0 and 5 mM glucose (v). Potentiometric signal obtained in AS at pH 7.4, on increasing the glucose concentration from 0 to 5 mM under a 250 kΩ load (vi). LSV curves (1 mV s^{-1}) for 0 and 1 mM glucose (vii). Potentiometric signal obtained in AS at pH 7.4 with 0.05 to 0.30 mM glucose under a 10 MΩ load (viii). **g**, Number of pixels corresponding to different glucose concentrations (i). Sweat glucose measured using the patch and the corresponding blood glucose level (ii). The patch displays in the 0–0.5 mM concentration range. On-body sweat glucose sensing on the subject's forearm and displaying 0.15 and 0.25 mM results by constant-load exercising (iii).

https://doi.org/10.1038/s41928-022-00843-6

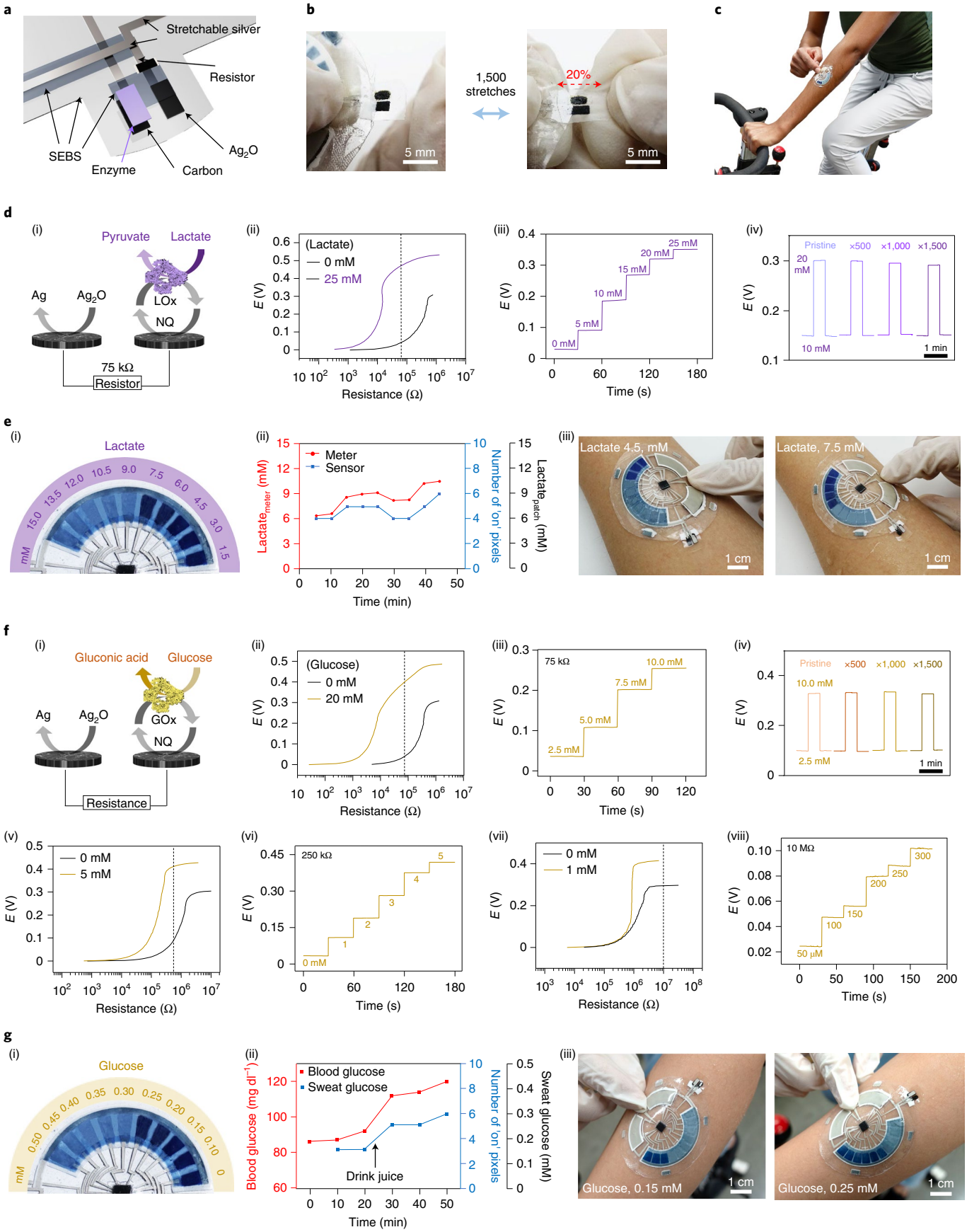

Methods

Chemicals

Graphite, toluene, acetone, ethanol, HCl, NQ, chitosan, glutaraldehyde, acetic acid, Nafion, lactatic acid, D-(+)-glucose, glucose oxidase, Ag flake, Ag_2O powder, Zn, ZnO, bismuth trioxide (Bi_2O_3), TiO_2, sodium ionophore X, sodium tetrakis[3,5-bis(trifluoromethyl)phenyl] borate, bis(2-ethylhexyl) sebacate, tetrahydrofuran (THF), polyvinyl butyral, poly(vinyl chloride), NaCl, SEBS-MA, methanol, iron (III) chloride, aniline, sodium phosphate anhydrous, citric acid, sodium PSS, glycerol, D-sorbital, acrylamide, *N*,*N*′-methylenebisacrylamide, potassium peroxydisulfate, sodium dodecylbenzene sulfonate and bromocresol green were purchased from Sigma-Aldrich. Polyurethane (Tecoflex EG-80A) was obtained from Lubrizol. SEBS G1645 triblock co-polymer was obtained from Kraton. Carboxyl-functionalized multi-walled carbon nanotube (MWCNT-COOH) was purchased from Cheap Tubes. The screen-printable PEDOT:PSS paste was purchased from Sun Chemical. LOx was purchased from Toyobo. Capstone fluorosurfactant FS-65 was purchased from DuPont. Poly(vinylfluoride-co-2,3,3,3-tetrafluoropropylene) binder (GBR6005) was obtained from Daikin.

Fabrication of stretchable circuit

A stretchable silver ink was used to fabricate the circuit that connects the various components of the device. The circuit pattern was designed with AutoCAD 2020 (Autodesk) and made into a cut-through metal stencil by Metal Etch Services. The stretchable silver ink was composed of silver flake, SEBS (40 wt% in toluene) and toluene in a 4:2:1 weight ratio.

After the printing of the silver ink layers, a chloride/lactic acid treatment, adapted from a previous study[39], was employed to further functionalize the silver particles and enhance the stability and conductivity of the silver layer during stretching. The treatment involved preparing an aqueous solution of 100 mM NaCl and 50 mM lactic acid, which was repeatedly sprayed onto the printed pattern using a spray bottle and dried in the oven at 80 °C for 5 min for three times, followed by washing with deionized (DI) water and drying in the oven at the same temperature for 10 min. The treatment endowed the silver layer with higher conductivity and stability (Supplementary Fig. 2). The subsequent PEDOT:PSS, Zn, Ag_2O and insulator can be printed on the treated silver layer.

Fabrication of ECD

The substrate for the ECD was composed of SEBS dissolved in toluene (40 wt%) and was fabricated by doctor blade casting (1,000 μm thick) the SEBS, followed by curing in the oven at 80 °C for 1 hour.

The ECD was fabricated using layer-by-layer screen printing with customized four kinds of ink: the electrochromic PEDOT:PSS ink, the silver ink for interconnection, the opaque insulator ink composed of SEBS and TiO_2 and the sodium-PSS-based electrolyte ink. The PEDOT:PSS ink was prepared using 1 g PEDOT:PSS paste, 0.2000 ml toluene, 0.1500 ml sodium dodecylbenzene sulfonate (75 mg ml^{-1} in DI water) and 0.0135 ml Capstone fluorosurfactant FS-65. The use of toluene enables better bonding between PEDOT:PSS and the substrate, and the addition of sodium dodecylbenzene sulfonate and Capstone surfactant was used to improve ink wettability to avoid contraction of the printed patterns due to surface tension of the ink. Furthermore, the addition of the surfactant can further improve PEDOT:PSS conductivity due to enhanced phase separation[46]. The opaque insulator ink was composed of TiO_2 and SEBS (40 wt% in toluene) in 1:10 weight ratio. The PSS electrolyte ink was formulated by mixing sodium PSS, D-sorbitol, glycerol, TiO_2 and polyacrylamide (PAM) precursor solution in a 4.0:1.0:1.0:0.8:2.0 weight ratio. The PAM solution was formulated by mixing acrylamide, DI water, potassium peroxydisulfate and *N*,*N*′-methylenebisacrylamide in a 2.00:10.00:0.05:0.02 ratio. Here TiO_2 was used to form a white, opaque electrolyte layer to enhance the colour-change contrast, whereas the PAM solution was used to enhance the electrolyte viscosity to avoid the bleeding and short-circuiting of the printed PSS electrolyte ink among the pixels (Supplementary Fig. 12). All the inks are mixed in the planetary mixer at 1,800 rpm for 10 min or until homogeneous.

The ECD panel was composed of the colour-changing top panel and the bottom panel to control the regional colour change. The PEDOT:PSS ink was printed first onto the SEBS substrate and cured in the oven at 100 °C for 2 hours. Then, the silver interconnection and opaque insulator layers were printed, with each layer cured at 80 °C for 5 min. Before assembly, the electrolyte was printed onto the bottom panel and briefly heated in the oven for 15 s at 80 °C to crosslink the PAM in the electrolyte.

Fabrication of stretchable battery

The formulation of the battery inks and electrolyte was adapted from previous studies[17,47]. The printing of the battery relied on four inks: Ag ink for the current collectors, Zn ink for the battery anode, Ag_2O ink for the battery cathode and separator ink for the battery separator. The Zn ink is prepared using Zn, ZnO, Bi_2O_3 and GBR6005 binder (25 wt% in acetone) in a 9.00:0.50:0.50:0.267 weight ratio. The Ag_2O ink was prepared using Ag_2O, Super P carbon black and GBR6005 binder (33 wt% in acetone) in a 1.90:0.10:2.66 weight ratio. The separator ink was composed of TiO_2, Triton X-114, SEBS (40 wt% in toluene) and toluene in a 3.0:0.1:1.5:1.5 weight ratio. All the inks were mixed in the planetary mixer at 2,500 rpm for 10 min or until homogeneous. The PVA electrolyte gel was initially crosslinked by dissolving 0.9 g PVA into 9.1 ml DI water at 90 °C, followed by mixing with 14.0 g of 16.7 wt% NaOH solution and desiccating the mixture in a vacuum desiccator until removing 67% of the total weight. The formed hydrogel was then cut using a three-dimensionally printed hole punch into the same shape as the electrodes and soaked in 9 M NaOH solution for over 12 hours before use. Here NaOH was used instead of potassium hydroxide to reduce self-discharge and extend the shelf life of the cell.

The stretchable battery was composed of two pairs of Ag_2O–Zn batteries separately printed on the bottom and top panels. The layer-by-layer printing steps of the battery were followed by using Ag ink, Zn anode or Ag_2O cathode ink, and separator ink, with each layer cured at 80 °C for 5 min (Supplementary Fig. 1). Before assembly, a PVA electrolyte gel was placed between the anode and cathode, and a concentric circle switch was placed between the Ag interconnection of two panels. After aligning and combining the two panels, the battery can effectively work and power the MCU by pressing the switch.

Fabrication of potentiometric sensors

The sodium and pH sensors were fabricated by using flexible silver and carbon inks. The formulation of the Ag ink is described above. The carbon ink was prepared using graphite, Super P carbon black, SEBS (40 wt% in toluene) and toluene in a 6.0:1.0:8.4:2.1 weight ratio. Both inks were mixed in a planetary mixer at 1,800 rpm for 10 min or until homogeneous.

The silver ink and carbon ink were printed onto the top-panel SEBS substrate in a layer-by-layer manner and were covered using SEBS resin to define the electrode area, exposing 2 mm^2 of carbon electrode as the working electrode and 1 mm^2 of the silver electrode as the reference electrode. A 0.1 M iron (III) chloride solution was drop cast onto the silver electrode to chlorinate the surface and form AgCl.

Fabrication of sodium sensor

The sodium sensor was based on screen-printed electrodes modified via drop casting. A cocktail composed of polyvinyl butyral (78.1 mg ml^{-1}) and NaCl (50.0 mg ml^{-1}) dissolved in methanol was drop cast onto the chlorinated reference surface (1.5 μl mm^{-2}). A polyurethane resin (1 g in 20 g THF) was then drop cast onto the dried cocktail layer (2 μl mm^{-2}) to prevent leaching. A cocktail for the Na^+-selective electrode was formulated by dissolving 1.00 mg sodium ionophore X, 0.77 mg sodium tetrakis[3,5-bis(trifluoromethyl)phenyl]borate ion exchanger, 33.00 mg poly(vinyl chloride) and 66.00 mg bis(2-ethylhexyl) sebacate in 660 ml

nitrogen-purged THF. The resulting cocktail was subsequently drop cast onto the carbon electrode (2 µl mm^{-2}).

Fabrication of pH sensor

Following the screen-printing fabrication protocol, the working and reference electrodes were created. The pH sensor was prepared by the electropolymerization of aniline onto the working carbon layer. The carbon electrode was first electrochemically cleaned via ten cyclic voltammetric scans in 0.5 M HCl (40 µl) from 0.3 to 1.1 V versus Ag/AgCl at a scan rate of 0.1 V s^{-1}. Subsequently, polyaniline electropolymerization was performed with a solution containing 0.1 M aniline in 1.0 M HCl by cyclic voltammetry from −0.2 to 1.0 V (versus Ag/AgCl) at 0.05 V s^{-1} to an accumulative gain of around 100 mC charge on the carbon electrode. Subsequently, the electrode was washed with DI water and was allowed to air dry.

Fabrication of enzymatic sensors

The glucose sensor and lactate sensor were fabricated by using flexible silver ink for the connection, carbon ink for the carbon enzymatic anode and Ag_2O ink for the sensor cathode. The Ag_2O ink is prepared by mixing Ag_2O, Super P carbon black and GBR binder (21 wt% in acetone) in a 1.900:0.100:3.166 weight ratio. The Ag_2O is mixed in a planetary mixer at 2,500 rpm for 10 min or until homogeneous.

The silver ink and carbon ink were printed onto the SEBS substrate in a layer-by-layer manner followed by printing the Ag_2O ink onto one of the carbon electrodes to obtain the cathode of both sensors. Finally, the electrodes were covered using SEBS resin to define the electrode area, exposing 2 mm^2 of carbon electrode as the anode and 2 mm^2 of the Ag_2O electrode as the cathode.

Modification of glucose sensor

The glucose sensor was fabricated by drop casting 0.2 M NQ solution dissolved in an acetone:ethanol (9:1) mixture containing 2 mg ml^{-1} MWCNT-COOH onto the carbon electrode (1.5 µl mm^{-2}). Then, 40 mg ml^{-1} glucose oxidase solution dissolved in phosphate-buffered saline (PBS) containing 10 mg ml^{-1} bovine serum albumin was drop cast after the first layer was dried (1.5 µl mm^{-2}). Finally, a 1.50 µl mm^{-2} chitosan layer (1 wt% in 0.1 M acetic acid) and a 0.75 µl mm^{-2} glutaraldehyde layer (1% in water) were drop cast on the top for improved immobilization. A surface-mount resistor (75 kΩ, 150 kΩ or 10 MΩ) was solvent welded between the two electrodes as the discharging load.

Modification of lactate sensor

The lactate sensor was fabricated similar to the glucose sensor; here 0.2 M NQ solution containing 2 mg ml^{-1} CNT-COOH (1.50 µl mm^{-2}) was drop cast, followed by 40 mg ml^{-1} LOx solution dissolved in PBS containing 10 mg ml^{-1} bovine serum albumin (1.50 µl mm^{-2}), as well as 1.50 µl mm^{-2} chitosan (1.0 wt% in 0.1 M acetic acid) and 0.75 µl mm^{-2} glutaraldehyde (0.5% in water) layer by layer after drying each layer. Finally, a 0.75 µl mm^{-2} poly(vinyl chloride) layer (3% in THF) was drop cast on the top for enzyme immobilization.

Device characterization and simulation

All the electrochemical measurements were performed on an Autolab PGSTAT204 potentiostat/galvanostat from Metrohm. All scanning electron microscopy imaging was performed on an FEI Quanta 250 FEG instrument. The AS was prepared in 0.1 M PBS considering major sweat constituents as additives: KCl (13 mM), NaCl (85 mM), lactate (17 mM) and urea (16 mM).

The fluid simulation was performed using Ansys 2022 R1, and a laminar flow was used in the model as the Reynold's number is less than 1. The simulation at the centre plane (50 µm from skin) was performed with two sweat rates: 30 nl min^{-1} cm^{-2} and 3 µl min^{-1} cm^{-2}, which correspond to the sweat rates at the stationary state and during exercise, respectively (Supplementary Fig. 24)[48,49].

Electrical circuit design

The control circuit was designed to digitalize the sensor output and control the ECD (Supplementary Fig. 22). An MCU (ATtiny441, Microchip Technology) with a 10 bit built-in ADC was used. The sensor voltage was first digitalized and then displayed by the 10 bit ECD. The sensor readout was mapped to the display bits as per their corresponding sensor calibration curve, and the ECD would address the individual pixels corresponding to the sensor voltage. The mapping of the ECD display and sensor voltage input is summarized in Supplementary Tables 1–6.

Assembly of self-powered sensing system

The MCU chip was placed onto the bottom panel after the procedure of screen printing above by the solvent-welding process to precisely connect with the Ag layer. A 5 µl droplet of toluene and ethanol (3:7 by volume) was used to temporarily soften the interconnecting silver traces followed by placing the MCU. The solvent was allowed to evaporate at room temperature for 5 min to facilitate the physical crosslinking of the SEBS within the Ag ink and the substrate to the metal contact pads of the MCU chip. This rapid solvent-welding process, thus, eliminates the use of any bonding layer or conductive paste. The connected MCU was sealed by 0.1 ml SEBS (40 wt% in toluene) and cured in the oven at 80 °C for 30 min after drying at room temperature. Two PVA gels were placed onto the Zn anode and Ag_2O cathode of the bottom panel as the electrolyte of the battery. The top panel was then aligned and covered with the bottom panel. Last, the assembled device was heat sealed on all the four sides to finish the device assembly.

On-body sensing with the patch

A stretchable adhesive (3M Adhesive Transfer Tape 468MP) was used to adhere the patch to the skin surface. A simple fluidic pattern was designed, allowing the adhesive layer to guide the sweat through the sensor and avoid sweat accumulation below the patch. The adhesive was initially cut using a computer-controlled cutter (Explore Air 2, Cricut) and attached to the back panel of the patch. The patch can thereafter be attached to the subject's arm during on-body trials. During the trial, the subject was asked to ride a stationary bike until sweating before applying the patch. To perform one sensing session, the subject can simply press the switch mechanism for ~1 s to refresh the display. To study the accuracy and temporal profile of sweat lactate, the sensing session was performed every 5 min, whereas the sweat on the other arm was collected and sensed using a commercial blood lactate meter (Lactate Plus, Nova Biomedical) as validation (Supplementary Fig. 25). To study the temporal profile of sweat glucose, the sensing session was performed every 10 min along with a blood-glucose fingerstick reading taken. After 20 min of exercise, the subject was asked to drink a sugary drink and exercise for 30 min more.

Data availability

The data that support the findings of this study are available from the corresponding author upon reasonable request.

Code availability

The code for programming the MCU is available from the corresponding author upon reasonable request.

References

1. Wang, C., Wang, C., Huang, Z. & Xu, S. Materials and structures toward soft electronics. *Adv. Mater.* **30**, 1801368 (2018).
2. Ray, T. R. et al. Bio-integrated wearable systems: a comprehensive review. *Chem. Rev.* **119**, 5461–5533 (2019).
3. Kang, J., Tok, J. B.-H. & Bao, Z. Self-healing soft electronics. *Nat. Electron.* **2**, 144–150 (2019).
4. Shih, B. et al. Electronic skins and machine learning for intelligent soft robots. *Sci. Robot.* **5**, eaaz9239 (2020).

5. Liu, Y., Pharr, M. & Salvatore, G. A. Lab-on-skin: a review of flexible and stretchable electronics for wearable health monitoring. *ACS Nano* **11**, 9614–9635 (2017).
6. Kim, J., Campbell, A. S., de Ávila, B. E.-F. & Wang, J. Wearable biosensors for healthcare monitoring. *Nat. Biotechnol.* **37**, 389–406 (2019).
7. Yang, Y. & Gao, W. Wearable and flexible electronics for continuous molecular monitoring. *Chem. Soc. Rev.* **48**, 1465–1491 (2019).
8. Gao, W., Ota, H., Kiriya, D., Takei, K. & Javey, A. Flexible electronics toward wearable sensing. *Acc. Chem. Res.* **52**, 523–533 (2019).
9. Gao, W. et al. Fully integrated wearable sensor arrays for multiplexed in situ perspiration analysis. *Nature* **529**, 509–514 (2016).
10. Emaminejad, S. et al. Autonomous sweat extraction and analysis applied to cystic fibrosis and glucose monitoring using a fully integrated wearable platform. *Proc. Natl Acad. Sci. USA* **114**, 4625–4630 (2017).
11. Chung, H. U. et al. Binodal, wireless epidermal electronic systems with in-sensor analytics for neonatal intensive care. *Science* **363**, eaau0780 (2019).
12. Manjakkal, L., Yin, L., Nathan, A., Wang, J. & Dahiya, R. Energy autonomous sweat-based wearable systems. *Adv. Mater.* **33**, 2100899 (2021).
13. Yin, L. et al. A self-sustainable wearable multi-modular E-textile bioenergy microgrid system. *Nat. Commun.* **12**, 1542 (2021).
14. Yin, L. et al. A passive perspiration biofuel cell: high energy return on investment. *Joule* **5**, 1888–1904 (2021).
15. Kim, D.-H. et al. Epidermal electronics. *Science* **333**, 838–843 (2011).
16. Kim, J. et al. Battery-free, stretchable optoelectronic systems for wireless optical characterization of the skin. *Sci. Adv.* **2**, e1600418 (2016).
17. Yin, L. et al. High performance printed AgO-Zn rechargeable battery for flexible electronics. *Joule* **5**, 228–248 (2021).
18. Occupational Safety and Health Administration. *Preventing Fire and/or Explosion Injury from Small and Wearable Lithium Battery Powered Devices*. (2016).
19. Kim, J. et al. Noninvasive alcohol monitoring using a wearable tattoo-based iontophoretic-biosensing system. *ACS Sens.* **1**, 1011–1019 (2016).
20. Song, Y. et al. Wireless battery-free wearable sweat sensor powered by human motion. *Sci. Adv.* **6**, eaay9842 (2020).
21. Kim, H.-J. et al. Review of near-field wireless power and communication for biomedical applications. *IEEE Access* **5**, 21264–21285 (2017).
22. Kim, E. H. et al. Organic light emitting board for dynamic interactive display. *Nat. Commun.* **8**, 14964 (2017).
23. Zhao, J. et al. A fully integrated and self-powered smartwatch for continuous sweat glucose monitoring. *ACS Sens.* **4**, 1925–1933 (2019).
24. Bandodkar, A. J. et al. Battery-free, skin-interfaced microfluidic/electronic systems for simultaneous electrochemical, colorimetric, and volumetric analysis of sweat. *Sci. Adv.* **5**, eaav3294 (2019).
25. Koh, A. et al. A soft, wearable microfluidic device for the capture, storage, and colorimetric sensing of sweat. *Sci. Transl. Med.* **8**, 366ra165 (2016).
26. Choi, J. et al. Soft, skin-integrated multifunctional microfluidic systems for accurate colorimetric analysis of sweat biomarkers and temperature. *ACS Sens.* **4**, 379–388 (2019).
27. Ghaffari, R. et al. Soft wearable systems for colorimetric and electrochemical analysis of biofluids. *Adv. Funct. Mater.* **30**, 1907269 (2020).
28. Aller-Pellitero, M. et al. Fully-printed and silicon free self-powered electrochromic biosensors: towards naked eye quantification. *Sens. Actuators B* **306**, 127535 (2020).
29. Sun, X. et al. A naked-eye readout self-powered electrochemical biosensor toward indoor formaldehyde: on-site detection and exposure risk warning. *Biosens. Bioelectron.* **177**, 112975 (2021).
30. Santiago-Malagón, S. et al. A self-powered skin-patch electrochromic biosensor. *Biosens. Bioelectron.* **175**, 112879 (2021).
31. Farahmand Nejad, M. A. et al. Electrochromism: an emerging and promising approach in (bio)sensing technology. *Mater. Today* **50**, 476–498 (2021).
32. Li, Z. & Suslick, K. S. Portable optoelectronic nose for monitoring meat freshness. *ACS Sens.* **1**, 1330–1335 (2016).
33. Gao, L. et al. Epidermal photonic devices for quantitative imaging of temperature and thermal transport characteristics of the skin. *Nat. Commun.* **5**, 4938 (2014).
34. Araki, H. et al. Materials and device designs for an epidermal UV colorimetric dosimeter with near field communication capabilities. *Adv. Funct. Mater.* **27**, 1604465 (2017).
35. Kim, J. et al. Ultrathin quantum dot display integrated with wearable electronics. *Adv. Mater.* **29**, 1700217 (2017).
36. Shi, X. et al. Large-area display textiles integrated with functional systems. *Nature* **591**, 240–245 (2021).
37. Miyamoto, A. et al. Inflammation-free, gas-permeable, lightweight, stretchable on-skin electronics with nanomeshes. *Nat. Nanotechnol.* **12**, 907–913 (2017).
38. Pu, X. et al. Wearable power-textiles by integrating fabric triboelectric nanogenerators and fiber-shaped dye-sensitized solar cells. *Adv. Energy Mater.* **6**, 1601048 (2016).
39. Lv, J. et al. Printable elastomeric electrodes with sweat-enhanced conductivity for wearables. *Sci. Adv.* **7**, eabg8433 (2021).
40. Jin, X. et al. Modeling, design guidelines, and detection limits of self-powered enzymatic biofuel cell-based sensors. *Biosens. Bioelectron.* **168**, 112493 (2020).
41. Derbyshire, P. J., Barr, H., Davis, F. & Higson, S. P. J. Lactate in human sweat: a critical review of research to the present day. *J. Physiol. Sci.* **62**, 429–440 (2012).
42. Buono, M. J., Lee, N. V. L. & Miller, P. W. The relationship between exercise intensity and the sweat lactate excretion rate. *J. Physiol. Sci.* **60**, 103–107 (2010).
43. ÅStrand, I. Lactate content in sweat. *Acta Physiol. Scand.* **58**, 359–367 (1963).
44. Baker, L. B. & Wolfe, A. S. Physiological mechanisms determining eccrine sweat composition. *Eur. J. Appl. Physiol.* **120**, 719–752 (2020).
45. Yin, L., Kim, K. N., Trifonov, A., Podhajny, T. & Wang, J. Designing wearable microgrids: towards autonomous sustainable on-body energy management. *Energy Environ. Sci.* **15**, 82–101 (2021).
46. Vosgueritchian, M., Lipomi, D. J. & Bao, Z. Highly conductive and transparent PEDOT:PSS films with a fluorosurfactant for stretchable and flexible transparent electrodes. *Adv. Funct. Mater.* **22**, 421–428 (2012).
47. Kumar, R. et al. All-printed, stretchable Zn-Ag_2O rechargeable battery via hyperelastic binder for self-powering wearable electronics. *Adv. Energy Mater.* **7**, 1602096 (2017).
48. Nyein, H. Y. Y. et al. A wearable patch for continuous analysis of thermoregulatory sweat at rest. *Nat. Commun.* **12**, 1823 (2021).
49. Kwon, K. et al. An on-skin platform for wireless monitoring of flow rate, cumulative loss and temperature of sweat in real time. *Nat. Electron.* **4**, 302–312 (2021).

Acknowledgements

L.Y. and K.N.K. recognize funding support from Samsung Display. K.N.K. recognizes funding from the National Research Foundation of

Korea (NRF-2018R1A6A3A03011252). We would like to thank Kraton Corporation for providing all the SEBS samples.

Author contributions

L.Y., K.N.K. and J.W. conceived the idea for this work. L.Y., M.C., K.N.K., A.T. and J.W. designed the experiments and wrote the manuscript. L.Y., M.C., J.-M.M., J.R.S., C.W., A.T., F.Z. and H.H. conducted the experiments. L.Y., M.C., J.Y. and R.L. fabricated the samples. M.L. designed and programmed the electronics. J.R.M. conducted the fluid simulations. A.T., J.G., S.X. and J.W. provided suggestions for the experiment designs. L.Y., M.C., K.N.K., J.R.S. and J.W. designed the figures and revised the manuscript.

Competing interests

The authors declare no competing interests.

Additional information

Supplementary information The online version contains supplementary material available at https://doi.org/10.1038/s41928-022-00843-6.

Correspondence and requests for materials should be addressed to Joseph Wang.

Peer review information *Nature Electronics* thanks the anonymous reviewers for their contribution to the peer review of this work.